Inorganic Chemistry
Article

Inorg. Chem. **2010**, *49*, 3113–3120 **3113**
DOI: 10.1021/ic901731b

Spectroscopic and Computational Studies of a μ-η^2:η^2-Disulfido-Bridged Dinickel(II) Species, [{(PhTt^{tBu})Ni}$_2$(μ-η^2:η^2-S$_2$)]: Comparison of Side-On Disulfido and Peroxo Bonding in (Ni^{II})$_2$ and (Cu^{II})$_2$ Species

Katherine M. Van Heuvelen,[†] Jaeheung Cho,[‡,§] Charles G. Riordan,[‡] and Thomas C. Brunold*[,†]

[†]*Department of Chemistry, University of Wisconsin—Madison, Madison, Wisconsin 53706, and* [‡]*Department of Chemistry and Biochemistry, University of Delaware, Newark, Delaware 19716.* [§]*Present address: Department of Chemistry and Nano Science, Ewha Womans University, Seoul 120-750, Korea.*

Received August 31, 2009

In this study, a combined spectroscopic and computational approach has been employed to generate a detailed description of the electronic structure of a binuclear side-on disulfido (Ni^{II})$_2$ complex, [{(PhTt^{tBu})Ni}$_2$(μ-η^2:η^2-S$_2$)] (**1**, where PhTt^{tBu} = phenyltris[(*tert*-butylthio)methyl]borate). The disulfido-to-Ni^{II} charge-transfer transitions that dominate the electronic absorption spectrum have been assigned on the basis of time-dependent density functional theory (DFT) calculations. Resonance Raman spectroscopic studies of **1** have revealed that the S−S stretching mode occurs at 446 cm^{-1}, indicating that the S−S bond is weaker in **1** than in the analogous μ-η^2:η^2-S$_2$ dicopper species. DFT computational data indicate that the steric bulk of PhTt^{tBu} stabilize the side-on core enough to prevent its conversion to the electronically preferred bis(μ-sulfido) (Ni^{III})$_2$ structure. Hence, **1** provides an interesting contrast to its O$_2$-derived analogue, [{(PhTt^{tBu})Ni}$_2$(μ-O)$_2$], which was shown previously to assume a bis(μ-oxo) (Ni^{III})$_2$ "diamond core". By a comparison of **1** to analogous disulfidodicopper and peroxodinickel species, new insight has been obtained into the roles that the metal centers, bridging ligands, and supporting ligands play in determining the core structures and electronic properties of these dimers.

I. Introduction

Metal−sulfur bonds are ubiquitous in metalloproteins, with sulfur deriving from active-site cysteine and methionine residues, inorganic sulfide, or sulfur-containing substrates.[1,2] In the case of nickel-containing proteins, sulfur ligation has been observed at the active sites of acetyl-CoA synthase/carbon monoxide dehydrogenase (ACS/CODH),[3−5] [NiFe] hydrogenase,[6] nickel superoxide dismutase,[7] and methyl-CoM reductase.[8] In order to expand our understanding of how sulfur ligation influences the electronic structures, and thus the reactivities, of these metalloproteins, some of us have synthesized nickel-containing model compounds with chelating thioether supporting ligands, such as the tridentate monoanion PhTt^{tBu} {PhTt^{tBu} = phenyltris[(*tert*-butylthio)methyl]borate}.[9−13] Early studies of nickel complexes possessing this ligand and derivatives thereof (PhTt^{R}) revealed that the identity of the R group plays a significant role in determining the geometry of the final product.[12] When R is a methyl (Me) group, monomeric species of the form [PhTt^{Me}]$_2$M (M = Fe, Co, Ni) have been obtained,[11] while sterically bulky R groups, such as *tert*-butyl, prevent the binding of a second supporting ligand and instead lead to the formation of pseudotetrahedral compounds, [PhTt^{tBu}]MCl (M = Co, Ni).[10] A four-coordinate nickel(I) complex of this type, [PhTt^{tBu}]Ni^{I}CO, has been shown to serve as a model of the putative Ni−CO intermediates in the catalytic cycle of ACS/CODH.[4]

*To whom correspondence should be addressed. E-mail: brunold@chem.wisc.edu.

(1) Solomon, E. I.; Szilagyi, R. K.; DeBeer George, S.; Basumallick, L. *Chem. Rev.* **2004**, *104*, 419–458.
(2) *Transition Metal Sulfur Chemistry: Biological and Industrial Significance*; American Chemical Society: Washington, DC, 1996.
(3) Brunold, T. C. *J. Biol. Inorg. Chem.* **2004**, *9*, 533–541.
(4) Craft, J. L.; Mandimutsira, B. S.; Fujita, K.; Riordan, C. G.; Brunold, T. C. *Inorg. Chem.* **2003**, *42*, 859–867.
(5) Ragsdale, S. W.; Kumar, M. *Chem. Rev.* **1996**, *96*, 2515–2539.
(6) Volbeda, A.; Charon, M.-H.; Piras, C.; Hatchikian, E. C.; Frey, M.; Fontecilla-Camps, J. C. *Nature* **1995**, *373*, 580–587.
(7) Fiedler, A. T.; Bryngelson, P. A.; Maroney, M. J.; Brunold, T. C. *J. Am. Chem. Soc.* **2005**, *127*, 5449–5462.
(8) Ermler, U.; Grabarse, W.; Shima, S.; Goubeaud, M.; Thauer, R. K. *Science* **1997**, *278*, 1457–1462.
(9) Chiou, S. J.; Innocent, J.; Riordan, C. G.; Lam, K. C.; Liable-Sands, L.; Rheingold, A. L. *Inorg. Chem.* **2000**, *39*, 4347–4353.
(10) Schebler, P. J.; Riordan, C. G.; Guzei, I. A.; Rheingold, A. L. *Inorg. Chem.* **1998**, *37*, 4754–4755.
(11) Ohrenberg, C.; Ge, P. H.; Schebler, P.; Riordan, C. G.; Yap, G. P. A.; Rheingold, A. L. *Inorg. Chem.* **1996**, *35*, 749–754.
(12) Ohrenberg, C.; Liable-Sands, L. M.; Rheingold, A. L.; Riordan, C. G. *Inorg. Chem.* **2001**, *40*, 4276–4283.
(13) Schebler, P. J.; Mandimutsira, B. S.; Riordan, C. G.; Liable-Sands, L. M.; Incarvito, C. D.; Rheingold, A. L. *J. Am. Chem. Soc.* **2001**, *123*, 331–332.

© 2010 American Chemical Society
Published on Web 03/03/2010

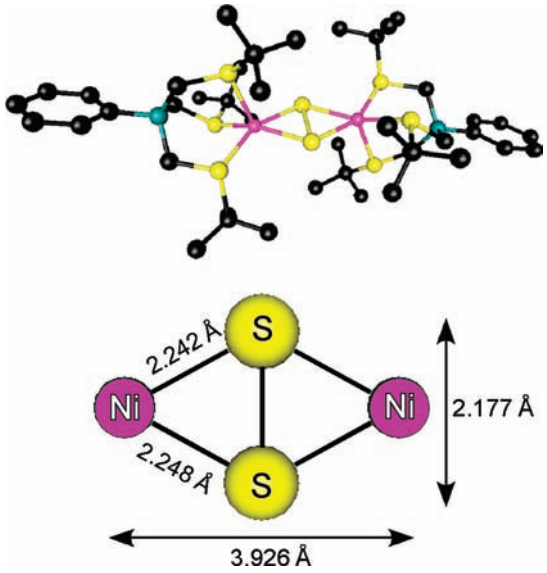

Figure 1. Crystal structure (top) and core dimensions (bottom) of **1**. H atoms are omitted for clarity.

Recently, we successfully prepared the dinickel(II) complex $[\{(PhTt^{tBu})Ni^{II}\}_2(\mu\text{-}\eta^2\text{:}\eta^2\text{-}S_2)]$ (**1**; Figure 1),[14] the disulfido analogue of $[\{(PhTt^{tBu})Ni^{III}\}_2(\mu\text{-}O)_2]$ (**2**) that we characterized previously.[15] X-ray crystallographic studies revealed that **1** is a side-on disulfido $(Ni^{II})_2$ dimer with a metal−metal separation of 3.93 Å (Figure 1),[14] while **2** was found to possess a bis(μ-oxo) $(Ni^{III})_2$ configuration with a significantly shorter Ni−Ni distance of 2.83 Å based on X-ray absorption spectroscopic data.[15,16] DFT computational results indicated that the bis(μ-oxo) core of **2** is significantly stabilized (by 32 kcal/mol) relative to its $\mu\text{-}\eta^2\text{:}\eta^2\text{-}O_2$ $(Ni^{II})_2$ counterpart.[15] These findings demonstrate that the bridging ligands drastically modulate the electronic structures and relative stabilities of the "diamond core" and side-on geometries of $[\{(PhTt^{tBu})Ni\}_2(L_2)]$ (L = O, S) species.

The interconversion between bis(μ-oxo) and side-on peroxo cores has been thoroughly investigated in the case of synthetic dicopper compounds,[17−19] particularly in terms of the effects of the supporting ligand on the $Cu_2(O_2)$ core structure. Steric bulk introduced by the supporting ligand can force the two metal centers apart, thereby favoring a side-on peroxo $(Cu^{II})_2$ structure. Conversely, strongly electron-donating ligands tend to stabilize the Cu^{III} state and, thus, the bis(μ-oxo) $(Cu^{III})_2$ core structure.[19] Other parameters such as the temperature, concentration, solvent polarity, and coordinating ability of the counterion can also influence the relative stabilities of the two core structures. At the electronic structural level, insight into the factors that govern the corresponding equilibrium has been obtained by an analysis of the frontier molecular orbitals (MOs).[19] As expected, increased back-bonding of the filled Cu 3d orbitals with the empty σ^* orbital of the O_2^{2-} moiety was found to promote reductive cleavage of the O−O bond, thereby driving the equilibrium toward the bis(μ-oxo) core.[19]

In comparison, the factors influencing the interconversion between the bis(μ-sulfido) and side-on disulfido core structures of $Cu_2(S_2)$ species are less well understood. Nevertheless, the electronic structures of side-on $Cu_2(S_2)$ complexes have been thoroughly characterized,[20−22] in particular by Solomon and co-workers, who performed a detailed study of $[\{HB(3,5\text{-}Pr^i{}_2pz)_3\}_2(Cu^{II})_2(\mu\text{-}\eta^2\text{:}\eta^2\text{-}S_2)]$ [**3**; $HB(3,5\text{-}Pr^i{}_2pz)_3$ = hydrotris(3,5-diisopropylpyrazolyl)borate].[23] The corresponding peroxo analogue of **3**, $[\{HB(3,5\text{-}Pr^i{}_2pz)_3\}_2Cu_2(O_2)]$ (**4**), also assumes a side-on $(Cu^{II})_2$ configuration. Significant back-bonding of the filled Cu 3d orbitals with the empty L_2 σ^* orbital (L = O, S) occurs in both species, weakening the L−L bond relative to end-on $Cu_2(L_2)$ compounds. However, this back-bonding interaction is insufficient to cause the L−L bond to break; hence, both **3** and **4** adopt side-on $(Cu^{II})_2$ core geometries. Similarly, in the preparation of $\mu\text{-}\eta^2\text{:}\eta^2\text{-}S_2$ dicopper complexes, Brown et al. found no evidence for the formation of any bis(μ-sulfido) $(Cu^{III})_2$ intermediates or degradation products.[24] Consistent with this finding, density functional theory (DFT) computational studies of hypothetical bis(μ-sulfido) $(Cu^{III})_2$ intermediates revealed that these species are significantly destabilized relative to their side-on disulfido $(Cu^{II})_2$ counterparts.[24]

While the electronic properties of side-on $Cu_2(S_2)$ species are relatively well understood, those of analogous $Ni_2(S_2)$ complexes remain largely unexplored. To fill this gap in our understanding of nickel sulfido species, we have recently initiated experimental and computational studies of dinickel compounds containing $Ni_2(S_2)$ cores. While a small number of nickel−sulfur dimers have been reported in the past,[25−30] herein we present the first rigorous characterization of the electronic and spectral properties of a complex possessing a side-on disulfido $(Ni^{II})_2$ core. Specifically, we have investigated **1** with electronic absorption (Abs), magnetic circular dichroism (MCD), and resonance Raman (rR) spectroscopic techniques as well as DFT and time-dependent DFT (TD-DFT) computational methods. Collectively, our results provide a detailed understanding of how the bridging and supporting ligands influence the electronic structure of **1** and provide insight into the factors that cause **1** to adopt a side-on disulfido $(Ni^{II})_2$ core structure while **2** assumes a bis(μ-oxo) $(Ni^{III})_2$ core geometry.

(14) Cho, J.; Van Heuvelen, K. M.; Yap, G. P. A.; Brunold, T. C.; Riordan, C. G. *Inorg. Chem.* **2008**, *47*, 3931–3933.
(15) Schenker, R.; Mandimutsira, B. S.; Riordan, C. G.; Brunold, T. *J. Am. Chem. Soc.* **2002**, *124*, 13842–13855.
(16) Mandimutsira, B. S.; Yamarik, J. L.; Brunold, T. C.; Gu, W.; Cramer, S. P.; Riordan, C. G. *J. Am. Chem. Soc.* **2001**, *123*, 9194–9195.
(17) Hatcher, L. Q.; Vance, M. A.; Sarjeant, A. A. N.; Solomon, E. I.; Karlin, K. D. *Inorg. Chem.* **2006**, *45*, 3004–3013.
(18) Mirica, L. M.; Ottenwaelder, X.; Stack, T. D. P. *Chem. Rev.* **2004**, *104*, 1013–1045.
(19) Henson, M. J.; Vance, M. A.; Zhang, C. X.; Liang, H.-C.; Karlin, K. D.; Solomon, E. I. *J. Am. Chem. Soc.* **2003**, *125*, 5186–5192.
(20) Bar-Nahum, I.; York, J. T.; Young, V. G. J.; Tolman, W. B. *Angew. Chem., Int. Ed.* **2007**, *47*, 533–536.
(21) Helton, M. E.; Maiti, D.; Zakharov, L. N.; Rheingold, A. L.; Porco, J. A.; Karlin, K. D. *Angew. Chem., Int. Ed. Engl.* **2006**, *45*, 1138–1141.
(22) Sarangi, R.; York, J. T.; Helton, M. E.; Fujisawa, K.; Karlin, K. D.; Tolman, W. B.; Hodgson, K. O.; Hedman, B.; Solomon, E. I. *J. Am. Chem. Soc.* **2008**, *130*, 676–686.
(23) Chen, P.; Fujisawa, K.; Helton, M. E.; Karlin, K. D.; Solomon, E. I. *J. Am. Chem. Soc.* **2003**, *125*, 6394–6408.
(24) Brown, E. C.; Aboelella, N. W.; Reynolds, A. M.; Aullon, G.; Alvarez, S.; Tolman, W. B. *Inorg. Chem.* **2004**, *43*, 3335–3337.
(25) Kruger, T.; Krebs, B.; Henkel, G. *Angew. Chem., Int. Ed. Engl.* **1989**, *28*, 61–62.
(26) Mealli, C.; Midollini, S. *Inorg. Chem.* **1983**, *22*, 2785–2786.
(27) Oster, S. S.; Lachicotte, R. J.; Jones, W. D. *Inorg. Chim. Acta* **2002**, *330*, 118–127.
(28) Pleus, R. J.; Waden, H.; Saak, W.; Haase, D.; Pohl, S. *J. Chem. Soc., Dalton Trans.* **1999**, 2601–2610.
(29) Tremel, W.; Henkel, G. *Inorg. Chem.* **1988**, *27*, 3896–3899.
(30) Mealli, C.; Midollini, S.; Sacconi, L. *Inorg. Chem.* **1978**, *17*, 632–637.

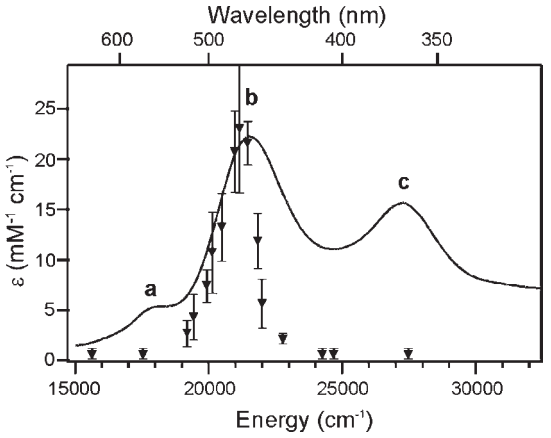

Figure 2. 298 K Abs spectrum (solid line) of **1** superimposed by the rR excitation profile for the ν_{S-S} vibrational feature observed at 446 cm^{-1}.

II. Experimental Section

II.A. Spectroscopy. Samples of **1** suitable for spectroscopic experiments were prepared in a 1:1 solution of $CHCl_3$/pentane as described in a previous report.[14] Room temperature Abs spectra were obtained on a Hewlett-Packard 8453 spectrophotometer equipped with a circulating water bath. Low-temperature Abs and MCD spectra of **1** were obtained using a Jasco J-715 spectropolarimeter in conjunction with an Oxford Instruments SM-4000 8T magnetocryostat. To eliminate contributions from glass strain to the MCD data, the −7 T spectrum was subtracted from the +7 T spectrum.

For rR studies, isotopically labeled samples of **1** in a $CHCl_3$ solution were prepared in NMR tubes, as described previously.[14] In addition, solid-state samples of **1** for rR experiments were prepared by thoroughly mixing ∼0.07 g of the sample with ∼0.30 g of KBr and a small amount of K_2SO_4, which was added as an internal standard. An Ar^+ ion laser (Coherent I-305) and a Kr^+ ion laser (Coherent I-302C) were used as the excitation sources, maintaining a power of 20−30 mW at the sample. Samples were placed in an electron paramagnetic resonance (EPR) dewar filled with liquid nitrogen to minimize photodecomposition. The scattered light was collected at a ∼135° backscattering angle from the surface of the sample and dispersed by a triple monochromator (Acton Research) with 1200 or 2400 grooves/mm gratings. Data were accumulated using a CCD camera (Princeton Instruments Spec X: 100 BR deep depletion, back-thinned, 1340 × 100 pixels). The 669 cm^{-1} peak of the $CHCl_3$ solvent and the 984 cm^{-1} feature of K_2SO_4 were used as internal standards for calibrating the frequencies and relative intensities of the rR features of solution and solid-state samples of **1**, respectively. To generate the rR spectrum of the solid-state sample shown in Figure 3, the baseline was modeled using a polynomial function that was subtracted from the raw data using the software package *Igor 4.08*.

II.B. Computations. II.B.1. Geometry Optimizations. All DFT geometry optimization studies were performed on a cluster of Intel Xeon processors (ACE computers) using the Amsterdam Density Functional (ADF) 2006 suite of programs.[31−34] For all atoms, ADF basis set IV (a triple-ζ basis set) was employed and core orbitals were frozen through 1s for C, N, and O and through 2p for Ni and S. The integration constant was set to 5.0, and the Vosko−Wilk−Nusair local density approximation[35] was used along with the nonlocal gradient corrections

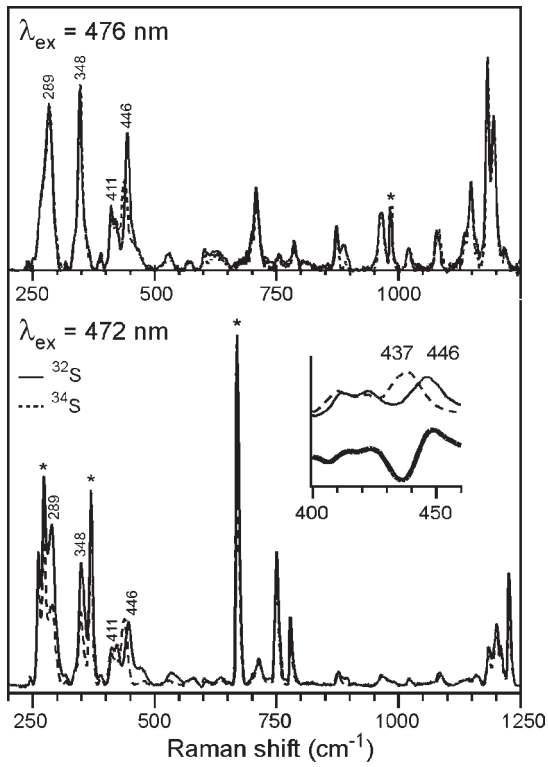

Figure 3. rR spectra of **1** obtained at 77 K with (top) 476 nm excitation for a solid-state sample and (bottom) 472 nm excitation for frozen-solution samples prepared with ^{32}S (solid line) and ^{34}S (broken line). The $CHCl_3$ solvent and K_2SO_4 internal standard peaks are marked with asterisks.

of Becke for exchange[36] and Perdew for correlation.[37] Atomic coordinates derived from the X-ray crystal structure of **1** served as the basis for generating three different computational models. Model **1a** consisted of the complete molecular structure of **1**. Alternatively, in model **1b**, the two terminal phenyl groups were substituted with methyl moieties, while in model **1c**, methyl groups replaced both the phenyl and the three *tert*-butyl groups in each $PhTt^{tBu}$ ligand. Both ferromagnetic [high spin (HS), $S = 2$] and antiferromagnetic [broken symmetry (BS), $M_S = 0$] exchange couplings were considered for each model.

II.B.2. Single-Point Calculations. The ORCA 2.6.35 software package developed by Dr. Frank Neese[38] was used to perform single-point DFT calculations on both the HS and BS states of the different models of **1**, in each case using the geometry-optimized model obtained for the BS state. Becke's three-parameter hybrid functional for exchange[39,40] and the Lee−Yang−Parr functional for correlation (B3LYP/G)[41] were used with the polarized-split-valence SV(P) basis[42] and the SV/C auxiliary basis[43] for all atoms except for the disulfido bridging ligand and Ni, for which Ahlrichs' polarized-triple-ζ-valence polarization (TZV) basis[44] was used with two and three polarization

(31) Velde, G. T.; Baerends, E. J. *J. Comput. Phys.* **1992**, *99*, 84–98.
(32) Versluis, L.; Ziegler, T. *J. Chem. Phys.* **1988**, *88*, 322–328.
(33) Baerends, E. J.; Ellis, D. E.; Ros, P. *Chem. Phys.* **1973**, *2*, 41.
(34) Guerra, C. F.; Snijders, J. G.; te Velde, G.; Baerends, E. J. *Theor. Chem. Acc.* **1998**, *99*, 391–403.
(35) Vosko, S. H.; Wilk, L.; Nusair, M. *Can. J. Phys.* **1980**, *58*, 1200–1211.
(36) Becke, A. D. *J. Chem. Phys.* **1986**, *84*, 4524–4529.
(37) Perdew, J. P. *Phys. Rev. B* **1986**, *33*, 8822–8824.
(38) Neese, F. *ORCA 2.6.35, an ab initio, density functional, and semi-empirical program package*; Max-Planck-Institut für Bioanorganische Chemie: Mülheim an der Ruhr, Germany, 2008.
(39) Becke, A. D. *J. Chem. Phys.* **1993**, *98*, 5648–5652.
(40) Becke, A. D. *J. Chem. Phys.* **1993**, *98*, 1372–1377.
(41) Lee, C. T.; Yang, W. T.; Parr, R. G. *Phys. Rev. B* **1988**, *37*, 785–789.
(42) Schafer, A.; Horn, H.; Ahlrichs, R. *J. Chem. Phys.* **1992**, *97*, 2571–2577.
(43) Weigend, F.; Haser, M. *Theor. Chem. Acc.* **1997**, *97*, 331–340.
(44) Schafer, A.; Huber, C.; Ahlrichs, R. *J. Chem. Phys.* **1994**, *100*, 5829–5835.

functions, respectively. All computations were performed as spin-unrestricted, with an integration grid of size 4 (302 Lebedev points). The BrokenSym keyword was employed to converge to the BS state.

II.B.3. TD-DFT Calculations. All TD-DFT calculations were performed with the ORCA 2.6.35 software package[45] using the functional and basis sets specified above for the single-point calculations. The TD-DFT results were used to simulate Abs spectra assuming that each electronic transition gives rise to a Gaussian band with a full width at half-maximum of $\nu_{1/2} = 1700$ cm^{-1}. The natures of key electronic transitions were explored on the basis of isosurface plots of MOs and electron density difference maps (EDDMs), which were obtained with the *gOpenMol* program developed by Laaksonen[46] using isodensity values of 0.03 and 0.003 au, respectively.

III. Results and Analysis

III.A. Spectroscopy. Two intense features dominate the Abs spectrum of **1** (Figure 2), exhibiting maxima at 27 320 cm^{-1} (ε = 15 000 M^{-1} cm^{-1}, band c) and 21 550 cm^{-1} (ε = 22 000 M^{-1} cm^{-1}, band b). Additionally, a shoulder is observed in the low-energy region at 18 180 cm^{-1} (ε = 4700 M^{-1} cm^{-1}, band a). In order to determine the nature of the electronic transitions responsible for these features, we conducted rR studies using laser excitation wavelengths spanning the entire visible spectral region (λ_{ex} = 407−676 nm). The rR spectra of **1** obtained upon excitation in resonance with the transition at 21 50 cm^{-1} (band b) show four intense peaks at 289, 348, 411, and 446 cm^{-1} (Figure 3). These vibrational features appear at virtually the same energies in both solid-state and frozen-solution samples, indicating that the molecular structure of **1** is preserved in the solvent mixture used. In order to identify the vibrations associated with these features, we performed additional rR experiments using a frozen-solution sample of **1** prepared with $^{34}S_8$. The 446 cm^{-1} peak shifted to 437 cm^{-1} (Δ = −9 cm^{-1}; Figure 3), in reasonable agreement with the calculated shift of Δ = −13 cm^{-1} for a S−S diatomic harmonic oscillator.[47] Therefore, we attribute the 446 cm^{-1} vibrational feature of **1** to the S−S stretching mode, ν_{S-S}, of the $Ni_2(S_2)$ core. In support of this assignment, the ν_{S-S} mode of the related $Cu_2(S_2)$ complex, **3**, is observed at 500 cm^{-1} (Δ = −12 cm^{-1}).[23]

The features at 289, 348, and 411 cm^{-1} are unaffected by $^{32}S \rightarrow {}^{34}S$ isotopic substitution and thus are not associated with vibrations that involve nuclear distortions of the disulfide moiety. Previous rR studies of **2** revealed vibrational features involving the $PhTt^{tBu}$ supporting ligand at 313, 363, and 415 cm^{-1}.[15] Therefore, it appears reasonable to assign the 348 and 411 cm^{-1} features of **1** as Ni−S(thioether) stretches. The assignment of the feature at 289 cm^{-1} is more ambiguous because it could be associated with a vibrational mode involving primarily Ni···Ni stretching motion (for comparison, ν_{Cu-Cu} of **3** occurs at 260 cm^{-1})[23] or a Ni−S(thioether) stretch.[15] To differentiate between these two possibilities, we performed a photodecomposition experiment in which the sample was irradiated at λ_{ex} = 476 nm with up to 150 mW at the sample to cause the partial degradation of **1**. While a marked loss of the intensity of the 446 cm^{-1} feature associated with the ν_{S-S} mode was observed in rR spectra collected afterward, the 289 and 348 cm^{-1} features did not notably decrease in intensity. Because photoexcitation at λ_{ex} = 476 nm should selectively destroy the side-on $Ni_2(S_2)$ core, and hence should result in the disappearance of both the ν_{Ni-Ni} and ν_{S-S} features, we assign the 289, 348, and 411 cm^{-1} bands as Ni−S(thioether) vibrations. Vibrational features in the correct range for the Ni···Ni stretching mode (i.e., 200−300 cm^{-1} based on a comparison to **3**)[23] did not decay in tandem with the ν_{S-S} stretching mode, thus precluding a definitive identification of the ν_{Ni-Ni} vibrational feature.

Table 1. Comparison of the Key Structural Parameters of the DFT-Optimized Computational Models (BS state) and Those Derived from the X-ray Crystal Structure of **1**

	1a	**1b**	**1c**	**1** (X-ray)
Ni−Ni (Å)	3.901	3.939	3.607	3.926
S−S (Å)	2.275	2.260	2.549	2.177
Ni−S (ave) (Å)	2.258	2.271	2.208	2.245
Ni−S−Ni (deg)	119.5	120.3	109.5	122.0
S−Ni−S (deg)	60.5	59.7	70.5	58.0

Variable-temperature MCD spectroscopic studies of **1** yielded a temperature-independent spectrum (Figure S3 in the Supporting Information), which is indicative of a diamagnetic species. This finding is consistent with previously reported EPR and ^{1}H NMR spectroscopic data of **1**.[14] Together, these results indicate that the ground state of **1** consists of two antiferromagnetically coupled HS Ni^{II} centers [note that the temperature dependence of the ^{1}H NMR data rules out the possibility that **1** consists of two low-spin (LS) Ni^{II} ions]. The nature of the ground state of **1** is explored in greater detail in section III.C.2.

III.B. Computations. To complement the spectroscopic studies presented above, we performed spin-unrestricted DFT calculations on models of **1** that considered two possible exchange-coupling schemes; namely, ferromagnetic coupling (HS, S = 2) and antiferromagnetic coupling (BS, M_S = 0) of two HS Ni^{II} centers. The X-ray crystal structure of **1** was used as the basis for generating a complete model of this species (defined as model **1a**).[14] Structural parameters obtained from a DFT geometry optimization of **1a** in the BS state agree reasonably well with those determined experimentally (Table 1). Importantly, the square-pyramidal coordination of the Ni center observed in the X-ray crystal structure is preserved in the energy-minimized model. To assess the importance of the steric constraints imposed by the $PhTt^{tBu}$ supporting ligand in **1**, two other computational models were considered in geometry-optimization studies. The two terminal phenyl groups were substituted with methyl moieties in model **1b**, whereas the methyl groups replaced both the phenyl and the three *tert*-butyl groups of each $PhTt^{tBu}$ ligand in model **1c** (Figure 4). While DFT energy minimizations of models **1a** and **1b** yielded optimized bond distances similar to those observed in the X-ray crystal structure of **1**, the Ni···Ni distance in model **1c** contracted by 0.3 Å and the S−S bond elongated by

(45) Neese, F. *ORCA 2.4.45, an ab initio, density functional, and semi-empirical program package*; Max-Planck-Institut für Bioanorganische Chemie: Mülheim an der Ruhr, Germany, 2005.
(46) Laaksonen, L. *J. Mol. Graphics* **1992**, *10*, 33–34.
(47) Spiro, T. G.; Czernuszewicz, R. S. Resonance Raman Spectroscopy. In *Physical Methods in Bioinorganic Chemistry: Spectroscopy and Magnetism*; Que, L., Ed.; University Science Books: Sausalito, CA, 2000; pp 59−119.

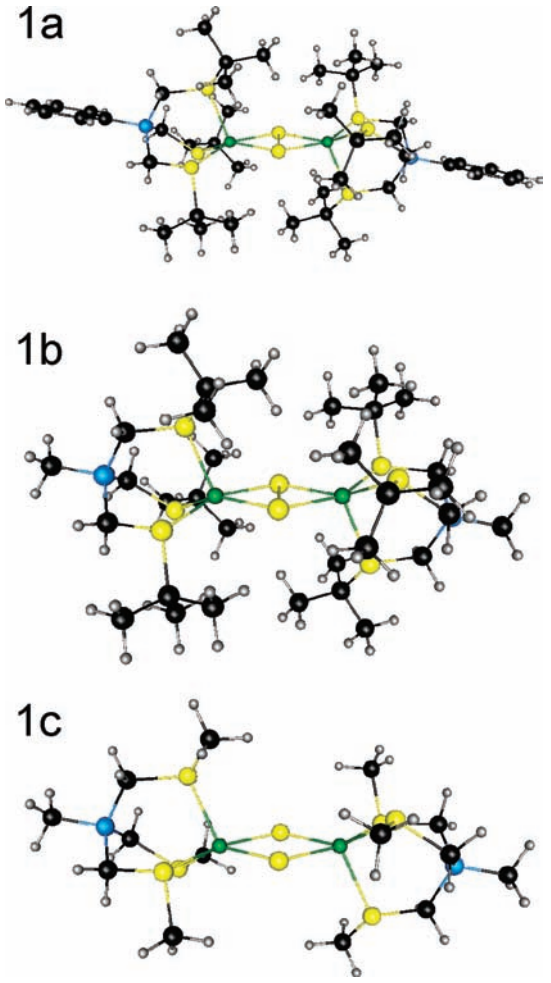

Figure 4. Computational models of **1** used to evaluate the influence of ligand steric effects on the core structure.

nearly the same amount, signifying a conversion from a side-on disulfido $(Ni^{II})_2$ to a bis(μ-sulfido) $(Ni^{III})_2$ core (Table 1). The implications of this result are explored further in section IV.C. Notably, the HS and BS coupling schemes resulted in significantly different energy-minimized geometries. While the BS approach yielded the geometries described above, geometry optimizations for the HS state converged to end-on *trans*-μ-1,2-S_2 $(Ni^{II})_2$ core structures for all three models. Thus, all subsequent calculations considered the optimized models obtained for the BS state.

III.C. Ground-State Properties. III.C.1. Nature of the Ni−S Bonds. In order to gain insight into the nature of the Ni−S bonding interactions, we performed spin-unrestricted BS ($M_S = 0$) single-point DFT calculations on model **1a**.[48] As revealed by the isosurface plots of the relevant spin-down (β) MOs shown in Figure 5, the BS formalism causes the spin-up (α) and β electrons to localize on opposite sides of the dimer. The highest occupied MO (HOMO) contains predominantly $S_2^{2-}(\pi^*_v)$ orbital character and minor contributions from the Ni *xy* orbitals [$S_2^{2-}(\pi^*_v)$ refers to the disulfido S 3p based orbital that is perpendicular to the $Ni_2(S_2)$ plane, while $S_2^{2-}(\pi^*_\sigma)$ denotes the disulfido S 3p based orbital that is contained within the $Ni_2(S_2)$ plane]. In contrast, the lowest unoccupied MO (LUMO) is primarily metal-based, with significant contributions from the Ni z^2 and Ni *xz* orbitals and minimal $S_2^{2-}(\pi^*_v)$ orbital character (Table 2). The considerable mixing of the Ni 3d orbitals with the frontier MOs of both the S_2^{2-} bridging moiety and the thioether supporting ligand is apparent in the HOMO−1 and LUMO+1 plots shown in Figure 5. These MOs formally derive from the $S_2^{2-}(\pi^*_\sigma)$ and Ni1 *xy* orbitals, respectively, but also contain significant contributions from the thioether supporting ligand. This DFT-predicted extensive mixing of metal and ligand orbitals in **1** is consistent with the rR enhancement of Ni−S(thioether) vibrational features for laser excitation in resonance with the $S_2^{2-} \rightarrow$ Ni charge transfer (CT) transition at 21 550 cm^{-1} (Figures 2 and S1 in the Supporting Information).

(48) Note that this model is distinct from computational model **1c**; for all single-point and TD-DFT studies, the experimentally observed side-on core geometry was preserved.

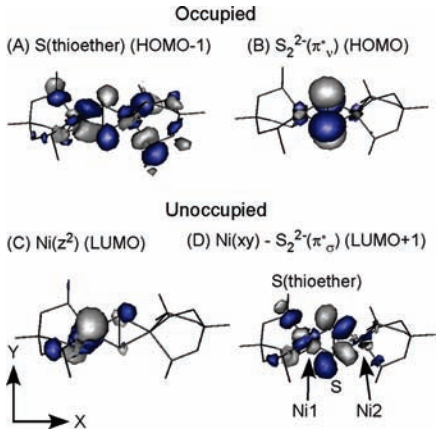

Figure 5. Isosurface plots of the β MOs involved in the dominant Abs transitions, as obtained from a BS DFT calculation on model **1a**.

Table 2. Energies (in eV) and Compositions (%) of the Ni 3d and Disulfido-Based β MOs, As Obtained from a BS DFT Calculation on Model **1a** (See Figure 5 for MO Plots)

E (eV)	MO[a]	occ.[b]	Ni1	S_2^{2-}	Ni2	$PhTt^{tBu}$
−2.10	Ni 3d (LUMO+1)	0	31 (*xy*)	30	7 (*xy*)	32
−2.43	Ni 3d (LUMO)	0	63 (39z^2, 24*xz*)	4	0	33
−5.34	S_2^{2-} (π^*_v) (HOMO)	1	5 (*yz*)	84	1 (*yz*)	10
−5.61	S(thioether) (HOMO−1)	1	5 (*xy*)	13	12	70

[a] Principal orbital contributor. [b] Occupancy of the MO.

III.C.2. Exchange Coupling. Both MCD and ^1H NMR spectral data reveal that **1** possesses a diamagnetic $S = 0$ ground state, indicating that the two Ni^{II} centers are antiferromagnetically coupled.[14] To estimate the magnitude of this exchange interaction, the coupling constant *J* was calculated using the Heisenberg−Dirac−Van Vleck Hamiltonian $H = -2J \cdot \mathbf{S}_1 \cdot \mathbf{S}_2$ (where $\mathbf{S}_1$ and $\mathbf{S}_2$ are the spin vectors for Ni centers 1 and 2, respectively) and the formalism derived by Noodleman (eq 1):[49]

$$J = \frac{-(E_{HS} - E_{BS})}{S_{max}^2} \quad (1)$$

From the total energies of model **1a** in the HS and BS states, E_{HS} and E_{BS}, respectively, and $S_{max}^2 = 4$, a value

(49) Noodleman, L. *J. Chem. Phys.* **1981**, *74*, 5737–5743.

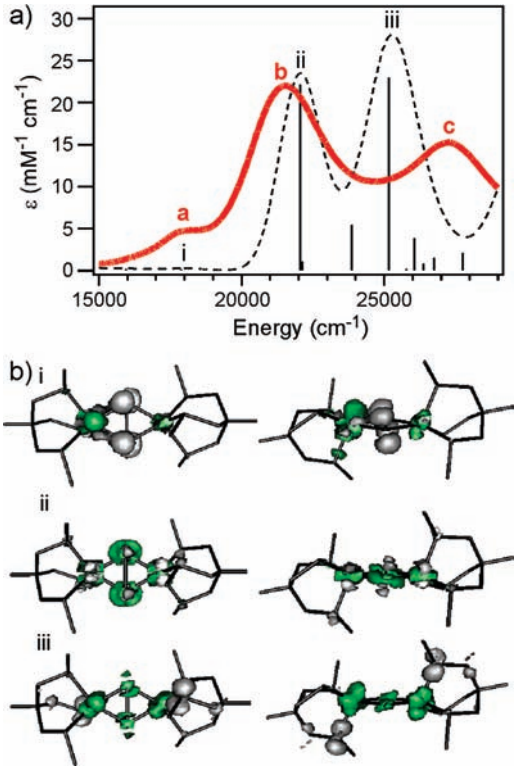

Figure 6. (a) TD-DFT-predicted (dashed line) and experimental (solid line) Abs spectra of **1**. The computed spectrum was obtained with model **1a** and with the BS formalism. (b) EDDMs showing the loss and gain of electron density (gray and green, respectively) for the three dominant calculated transitions (top and front views are shown on the left and right, respectively).

of $J = -1595\ cm^{-1}$ was obtained. This value is larger than the experimental value of $-476\ cm^{-1}$ estimated from variable-temperature ^1H NMR studies,[14] suggesting that our DFT calculations somewhat overestimate the Ni−S bond covalency in **1**. Antiferromagnetic coupling arises from delocalization of the unpaired electron spin density from the Ni1 3d orbitals into the half-filled 3d orbitals of Ni2, and vice versa, via the π^*_σ orbital of the bridging disulfido moiety. According to Table 2 and Figure 5, the dominant superexchange pathway is thus comprised of the Ni *xy* orbitals that are σ-antibonding with respect to the $S_2^{2-}(\pi^*_\sigma)$ orbital (the LUMO+1).[50]

III.D. Excited States. TD-DFT Calculations and Spectral Assignments. TD-DFT calculations were carried out to assign the dominant features in the Abs spectrum of **1** and identify the donor and acceptor MOs involved in the corresponding electronic transitions. All TD-DFT calculations were performed on model **1a** described in section III.C.1 and employing the BS formalism to account for the experimentally observed, and computationally predicted, antiferromagnetic coupling of the two HS Ni^{II} centers in **1**.

The experimental Abs spectrum of **1** displays three features (bands a−c in Figure 6) that had tentatively been attributed to ligand-to-metal CT transitions on the basis of a comparison to **3**.[14] These assignments are corroborated by the rR data of **1** obtained in the present study (vide supra). Consistent with these experimental data, the TD-DFT-calculated Abs spectrum for model **1a** (Figure 6) shows two dominant features at 22 050 cm^{-1} (band ii, $\varepsilon = 22\,170\ M^{-1}\ cm^{-1}$) and 25 170 cm^{-1} (band iii, $\varepsilon = 22\,950\ M^{-1}\ cm^{-1}$), as well as a weak feature at lower energy (band i, $\varepsilon = 150\ M^{-1}\ cm^{-1}$). The EDDMs shown in Figure 6 provide a pictorial representation of the charge redistributions accompanying the transitions associated with bands i−iii. The low-energy band i, which is the counterpart of band a in the experimental Abs spectrum, arises from a $S_2^{2-} \rightarrow Ni^{II}$ CT transition in which electron density shifts primarily from the disulfido(π^*_ν) to the Ni z^2 orbitals. An analysis of the TD-DFT results for the transition responsible for band ii shows that the electron density is mainly donated from orbitals of predominantly $S_2^{2-}(\pi^*_\sigma)$ and S(thioether) character, namely, HOMO−3 and HOMO−1 to LUMO+1, leading to the assignment of band ii and its experimental counterpart, band b, as a $S_2^{2-}(\pi^*_\sigma) \rightarrow Ni^{II}$ CT transition. Because the LUMO also contains significant $S_2^{2-}(\pi^*_\sigma)$ character, the corresponding EDDM additionally shows some out-of-plane to in-plane CT character. The mixing of S_2^{2-} and S(thioether) orbital character in the donor orbitals is consistent with the observed rR enhancement of both ν_{S-S} and $\nu_{Ni-S(thioether)}$ vibrational modes upon laser excitation into band b (Figures 2 and S1 in the Supporting Information). Finally, the EDDM for the transition associated with the highest-energy band iii reveals that this transition is best described as involving S(thioether)/$S_2^{2-}(\pi^*_\nu) \rightarrow Ni^{II}$ CT excitation. This assignment is nicely corroborated by the rR spectrum obtained with 364 nm laser excitation (Figure S2 in the Supporting Information), which shows predominant enhancement of a Ni−S(thioether) vibration at 411 cm^{-1}.

IV. Discussion

IV.A. Spectral and Electronic Properties of 1. While in many respects the spectral features of **1** are strikingly similar to those reported for side-on disulfido $(Cu^{II})_2$ complexes, the results presented herein suggest that the metal center and supporting ligand play an important role in modulating the bonding interactions and, thus, the spectral properties of species containing a μ-η^2:η^2-S_2M_2 core (M = Ni^{II}, Cu^{II}). Collectively, ^1H NMR and MCD spectroscopic data and DFT computational results indicate that **1** features two antiferromagnetically coupled HS Ni^{II} centers, with the $S_2^{2-}(\pi^*_\sigma)$ orbital serving as a highly efficient superexchange pathway between the Ni *xy* orbitals. The rR spectrum of **1** shows considerable enhancement of the ν_{S-S} and $\nu_{Ni-S(thioether)}$ vibrational modes upon laser excitation in resonance with the dominant electronic transition at 21 550 cm^{-1} (Figure 2). These rR data, in conjunction with the TD-DFT computational results, allow the three dominant features in the visible region of the Abs spectrum of **1** to be assigned as $S_2^{2-} \rightarrow Ni^{II}$ CT transitions.

To establish the basis for a quantitative comparison between the metal−ligand bonding interactions in **1** and related $M_2(S_2)$ dimers, we considered performing a normal-coordinate analysis on the $Ni_2(S_2)$ core of **1**. Treating this four-atom core with idealized D_{2h} symmetry and ignoring the out-of-plane mode yields five in-plane vibrational modes, $2a_g + b_{1g} + b_{2u} + b_{3u}$. Of these, only the two totally symmetric vibrational modes corresponding to the

(50) Because this MO is empty, delocalizaton of the hole character from Ni1 onto Ni2 reflects the extent of electron delocalization from Ni2 onto Ni1 in the corresponding Ni2 *xy* based occupied MO.

ν_{S-S} and ν_{Ni-Ni} stretches are expected to show significant rR enhancement. The former is observed at 446 cm^{-1}, while the ν_{Ni-Ni} feature cannot be assigned conclusively based on the rR results reported above. Consequently, there are insufficient data to conduct a normal-coordinate analysis and quantify the core bond strengths of **1**.

Nonetheless, valuable information about the strength of the Ni−S bonding interactions in **1** can be obtained by using Badger's rule, which relates an observed vibrational frequency to the corresponding bond length according to eq 2:[51]

$$r_e = \frac{C_{ij}}{\nu_e^{2/3}} + d_{ij} \qquad (2)$$

r_e is the bond length (here, r_{S-S}), ν_e is the experimental Raman frequency of the normal mode in question (i.e., ν_{S-S}), and C_{ij} and d_{ij} are empirical constants. Using ν_e = 446 cm^{-1} from our rR data and the published values C_{S-S} = 63.95 and d_{S-S} = 1.063 in eq 2,[52,53] we obtain a S−S distance of 2.16 Å, in excellent agreement with the disulfido bond length of 2.1776 Å observed in the X-ray crystal structure of **1**. Consequently, the frequency of ν_{S-S} by itself provides a useful measure for a comparison of the S−S bond strength in **1** and related $M_2(S_2)$ dimers (see below).

IV.B. Comparison to 3. The Abs spectrum of **3** is dominated by an intense band at 28 000 cm^{-1} (ε = 31 200 M^{-1} cm^{-1}) with a low-energy shoulder at 21 000 cm^{-1} (ε = 3700 M^{-1} cm^{-1}), which were assigned as $S_2^{2-}(\pi^*_\sigma) \rightarrow Cu^{II}$ and $S_2^{2-}(\pi^*_\nu) \rightarrow Cu^{II}$ CT transitions, respectively, on the basis of their positions and intensities, as well as rR data.[23] Additionally, two less intense features at 15 000 cm^{-1} (ε = 230 M^{-1} cm^{-1}) and 10 300 cm^{-1} (ε = 130 M^{-1} cm^{-1}) were attributed to Cu^{II} d → d transitions. In the case of **1**, the most intense Abs feature (Figure 2) is observed at 21 550 cm^{-1} (ε = 17 500 M^{-1} cm^{-1}) and displays a shoulder at 18 180 cm^{-1} (ε = 3800 M^{-1} cm^{-1}). Consequently, both the $S_2^{2-}(\pi^*_\sigma) \rightarrow Ni^{II}$ and $S_2^{2-}(\pi^*_\nu) \rightarrow Ni^{II}$ CT transitions occur at lower energy than their $S_2^{2-} \rightarrow Cu^{II}$ counterparts in **3**.

The ν_{S-S} vibrational mode appears at lower frequency in **1** (446 cm^{-1}) than in **3** (500 cm^{-1}), suggesting that the S−S bond in the $Ni_2(S_2)$ species is substantially weaker than the disulfido bond in the dicopper complex.[47] Although, in principle, a normal-coordinate analysis must be performed to determine bond strengths because of the influence of mechanical coupling on the frequency of vibrational modes,[54] the close correspondence between the S−S bond distances for **1** predicted by Badger's rule (eq 2) and determined by X-ray crystallography suggests that the ν_{S-S} modes in this dimer and related $M_2(S_2)$ compounds contain comparable S−S stretching character (note that the application of Badger's rule to the vibrational data of **3** yielded an estimated S−S bond distance of 2.078 Å, in excellent agreement with the DFT-optimized value of 2.072 Å[23]). Thus, the higher frequency of the ν_{S-S} feature of **3** relative to **1** is consistent with the shorter DFT-optimized S−S distance for **3** of 2.076 Å,[23] as compared to 2.275 Å in model **1a** (DFT) and 2.178 Å in **1** (X-ray structure). In part, this difference can be attributed to the lower effective nuclear charge of Ni versus Cu, which promotes increased charge donation from the filled Ni 3d based MOs into the $S_2^{2-}(\sigma^*)$ orbital. However, it is likely that the difference in the supporting ligands of **1** and **3** (a tridentate thioether and a tridentate pyrazole, respectively) also makes a significant contribution to the stronger S−S bond in the dicopper species. Specifically, studies of side-on $Cu_2(S_2)$ compounds have revealed that supporting ligands that act as strong electron donors tend to increase the extent of back-bonding between the metal and the disulfido moiety, thus causing a weakening of the S−S bond.[53] Because the frontier MOs of the thioether supporting ligand are in fairly close energetic proximity to the Ni 3d and S_2^{2-} orbitals in **1**, they greatly enhance the degree of back-bonding interactions and, consequently, weaken the S−S bond [see Figure S5 for a plot of the $S_2^{2-}(\sigma^*)$-based MO]. In comparison, the $Cu_2(S_2)$ core orbitals of **3** are relatively unperturbed by the more weakly electron-donating pyrazole supporting ligand.

IV.C. Comparison of Side-On and End-On $Ni_2(S_2)$ Cores. As described in the preceding paper, we have carried out a parallel investigation of an end-on $Ni_2(S_2)$ dimer, [{(tmc)Ni}$_2$(*trans*-μ-1,2-S_2)](OTf)$_2$ (**5**; tmc = 1,4,8,11-tetramethyl-1,4,8,11-tetraazacyclotetradecane) using the same spectroscopic and computational methods that we employed in this study.[55,56] As in **1**, antiferromagnetic coupling of two HS Ni^{II} centers in **5** results in a diamagnetic ground state. A moderately intense $S_2^{2-} \rightarrow Ni^{II}$ CT band at 15 500 cm^{-1} dominates the Abs spectrum of **5** (ε > 4000 M^{-1} cm^{-1}). rR studies using laser excitation in resonance with this $S_2^{2-} \rightarrow Ni^{II}$ CT transition led to identification of the ν_{S-S} and ν_{Ni-S} stretches at 474 and 273 cm^{-1}, respectively. A normal-coordinate analysis of these data revealed that the S−S and M−S bonds in **5** are weaker than those in a similar end-on disulfidodicopper species, [{(TMPA)Cu}$_2$(S_2)]$^{2+}$ [**6**; TMPA = tris(2-pyridylmethyl)amine],[23] in close analogy to the weaker bonding within the $M_2(S_2)$ cores of **1** versus **3** (vide supra).

The Ni−S bonds in **1** and **5** contain 34% and 15% S 3p orbital character, respectively, as inferred from the DFT-computed compositions of the corresponding LUMO and LUMO+1 orbitals.[57] This difference in the computed Ni−S bond covalency is in qualitative agreement with the increased absorption intensity of the dominant $S_2^{2-} \rightarrow Ni^{II}$ CT bands in **1** compared to **5** (ε = 22 000 and > 4000 M^{-1} cm^{-1}, respectively). Similarly, previous spectroscopic and computational studies of the side-on $Cu_2(S_2)$ species **3** and the end-on $Cu_2(S_2)$ species **6** revealed that the Cu−S bonds in **3** are roughly twice as covalent as those in **6**.[23] This difference can be understood by considering how the core geometry modulates the extent of disulfido-to-nickel charge donation. In **5**, each Ni center interacts with a single S atom of the disulfido moiety,

(51) Badger, R. M. *J. Chem. Phys.* **1935**, *3*, 710–714.

(52) These constants were obtained from a previous report that invoked Badger's rule to correlate experimental ν_{S-S} vibrational frequencies with S−S bond lengths for a series of side-on $M_2(S_2)$ complexes (M = Cu, Mo, Ir, Fe, Ru, Nb).

(53) Brown, E. C.; Bar-Nahum, I.; York, J. T.; Aboelella, N. W.; Tolman, W. B. *Inorg. Chem.* **2007**, *46*, 486–496.

(54) Brunold, T. C.; Tamura, N.; Kitajima, N.; Moro-oka, Y.; Solomon, E. I. *J. Am. Chem. Soc.* **1998**, *120*, 5674–5690.

(55) Kieber-Emmons, M. T.; Van Heuvelen, K. M.; Brunold, T. C.; Riordan, C. G. *J. Am. Chem. Soc.* **2009**, *131*, 440–441.

(56) Van Heuvelen, K. M.; Kieber-Emmons, M. T.; Riordan, C. G.; Brunold, T. *Inorg. Chem.*, submitted for publication.

(57) These values were obtained from the S_2^{2-} contributions to the LUMO and LUMO+1 orbitals (Table 2).

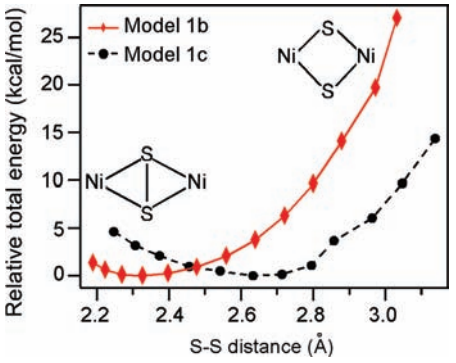

Figure 7. Variation of the relative total energy upon conversion of the core structures of models **1b** (diamonds) and **1c** (circles) from a μ-η^2:η^2-S_2 to a bis(μ-sulfido)dinickel geometry.

whereas in **1**, each Ni center experiences direct orbital overlap with both bridging S atoms. This results in a significant increase in the overall Ni−S bond covalency in the side-on structure relative to the end-on configuration.

IV.D. Effects of Supporting Ligands and Comparison to 2. In an effort to assess the steric and electronic effects of the PhTt^{tBu} supporting ligand on the core geometry of **1**, we performed DFT geometry optimizations on the three different computational models described in section III.B (Figure 4). In each case, the BS formalism was used to account for the experimentally observed $S = 0$ ground state. While DFT geometry optimizations of models **1a** and **1b** retained the Ni−Ni distance of ~3.9 Å observed by X-ray crystallography, the Ni−Ni separation dropped by 0.3 Å and the S−S distance increased by the same amount upon optimization of model **1c**, signifying a conversion from a side-on disulfido $(Ni^{II})_2$ to a bis(μ-sulfido) $(Ni^{III})_2$ geometry (Table 1). Recently, Hoffmann and co-workers proposed that relatively long S−S distances (~2.75 Å) reflect a formal bond order of 0.5,[58,59] which raises the possibility that **1c** (calcd S−S distance of 2.55 Å) could be described as a mixed-valence complex, e.g., $Ni^{III}Ni^{II}(S_2^{3-})$. However, an analysis of the DFT-computed MOs of **1c** reveals two Ni^{III} centers and supports a bis(μ-sulfido) $(Ni^{III})_2$ description for this model.

To understand this change in the core structure between models **1b** and **1c**, a DFT geometry optimization study was performed in which the Ni−Ni distance was varied systematically in fixed increments of 0.1 Å (from 4.03 to 2.93 Å) and all other internal coordinates were allowed to relax.[60] The resulting total energy profiles show that model **1b** strongly favors a relatively short S−S bond (r_{Ni-Ni} = 3.83 Å and r_{S-S} = 2.33 Å) associated with a side-on core geometry. In contrast, model **1c** prefers to adopt a bis(μ-sulfido) $(Ni^{III})_2$ core, with a Ni−Ni separation that is a full 0.3 Å shorter than that favored by **1b** (r_{Ni-Ni} = 3.53 Å and r_{S-S} = 2.63 Å; Figure 7). These results suggest that the bis(μ-sulfido) $(Ni^{III})_2$ configuration is preferred on the basis of electronic factors, while the steric bulk of the PhTt^{tBu} ligand of **1** favors the longer metal−metal separation associated with the observed μ-η^2:η^2 geometry. Importantly, while similar computational studies on related $Cu_2(S_2)$ dimers revealed a prohibitively large energy barrier for the conversion of a μ-η^2:η^2-S_2 to a bis(μ-sulfido)dicopper core geometry,[24,61] our results suggest that removal of the steric bulk of the PhTt^{tBu} supporting ligand should permit access to an unprecedented $(Ni^{III})_2(\mu\text{-}S)_2$ species.

A similar DFT study that considered the conversion of **2** to a putative side-on peroxo derivative [{(PhTt^{tBu})Ni^{II}}$_2$-(μ-η^2:η^2-O_2)] revealed that the $(Ni^{III})_2(\mu\text{-}O)_2$ structure is stabilized by 32 kcal/mol relative to the μ-η^2:η^2-O_2 $(Ni^{II})_2$ core despite the steric bulk of the PhTt^{tBu} ligand.[15] These computational studies indicated that an increase in the O−O bond distance enhances the σ-bonding interaction between the Ni xy and O_2^{2-}(σ*) orbitals.[15] Because the peroxo (σ*) orbital is in close energetic proximity to the Ni 3d orbitals, the extent of back-bonding is sufficiently large to cause the O−O bond to break and thus to stabilize the Ni^{III} oxidation state inherent to the bis(μ-oxo) configuration. In contrast, the disulfido (σ*) orbital in **1** is significantly destabilized relative to the Ni 3d orbitals because of the lower electronegativity of S as compared to O. This large energy gap is not conducive to extensive back-donation of the electron density from the Ni 3d orbitals to the S_2^{2-}(σ*) orbital necessary to cleave the S−S bond [the S_2^{2-}(σ*)-based MO showing this back-bonding interaction is depicted in Figure S5 in the Supporting Information]. Consequently, **1** assumes the observed side-on configuration.

V. Conclusions

In this study, we have carried out a detailed characterization of the geometric and electronic structures of **1**. The extensive mixing of the Ni 3d orbitals with both the disulfido and thioether frontier MOs strongly affects the key spectroscopic properties of **1**, decreasing the frequency of ν_{S-S} and giving rise to the rR enhancement of Ni−S(thioether) vibrational features upon excitation in resonance with $S_2^{2-} \rightarrow Ni^{II}$ CT transitions. The highly covalent Ni−S bonding interactions create an efficient superexchange pathway for mediating strong antiferromagnetic exchange coupling, as demonstrated by the large magnitude of the coupling constant J. The side-on core geometry observed for **1** is favored by the low electronegativity of S, which significantly destabilizes the S_2^{2-}(σ*) orbital and hence prevents the degree of back-bonding interaction needed to cleave the S−S bond, and to a lesser degree by the steric bulk of the PhTt^{tBu} supporting ligand, which favors a longer Ni−Ni separation.

Acknowledgment. This work has been supported by the NSF Graduate Research Fellowship program (to K.M.V.H.) and by the NSF (Grants CHE-0518508 and CHE-0809603 to C.G.R.). We thank Professor Frank Neese, Universität Bonn, for providing us with a free copy of ORCA.

Supporting Information Available: Atomic coordinates of the geometry-optimized models **1a**−**1c** (Tables S1−S3), additional rR data (Figures S1 and S2), MCD data (Figure S3), a plot of the S−S bond length as a function of the Ni−Ni separation in model **1b** (Figure S4), and a plot of the S_2^{2-}(σ*)-based MO (Figure S5). This material is available free of charge via the Internet at http://pubs.acs.org.

(58) Mealli, C.; Ienco, A.; Poduska, A.; Hoffmann, R. *Angew. Chem., Int. Ed.* **2008**, *47*, 2864–2868.
(59) Poduska, A.; Hoffmann, R.; Ienco, A.; Mealli, C. *Chem. Asian J.* **2009**, *4*, 302–313.
(60) Because energy-minimized models of **1a** and **1b** both preserved the side-on core, model **1b** is considered herein for computational practicality.
(61) Aullón, G.; Alvarez, S. *Eur. J. Inorg. Chem.* **2004**, 4430–4438.